# Vibrational response of clusters of $Fe_3O_4$ nanoparticles patterned on glass surfaces investigated with magnetic sample modulation AFM

| | |
|---|---|
| Journal: | *Nanoscale* |
| Manuscript ID | NR-ART-07-2018-006174.R1 |
| Article Type: | Paper |
| Date Submitted by the Author: | 05-Oct-2018 |
| Complete List of Authors: | Kulkarni, Shalaka; Louisiana State University, Department of Chemistry<br>Kolhatkar, Arati; University of Houston, Department of Chemistry<br>Lee, T. Randall; University of Houston, Department of Chemistry<br>Garno, Jayne; Louisiana State University, Department of Chemistry |
| | |

For RSC *Nanoscale*

# Vibrational response of clusters of $Fe_3O_4$ nanoparticles patterned on glass surfaces investigated with magnetic sample modulation AFM

Shalaka A. Kulkarni,[a] Arati G. Kolhatkar,[b] T. Randall Lee[b] and Jayne C. Garno[a]*

[a] Department of Chemistry, Louisiana State University, 232 Choppin Hall, Baton Rouge, LA, 70803 USA

[b] Department of Chemistry and Texas Center for Superconductivity, University of Houston, Houston, TX 77204-5003, USA

Corresponding author: Jayne C. Garno
Phone: 225-578-8942
Fax: 225-578-3458
E-mail: jgarno@lsu.edu

## Abstract

The vibration of $Fe_3O_4$ nanoparticles in response to an alternating magnetic field can be sensitively detected using contact mode atomic force microscopy (AFM) combined with selective modulation of magnetic domains. While imaging patterned samples of magnetic nanoparticles with contact mode AFM, a magnetic field was applied to drive sample vibration. The field altered in polarity and strength according to parameters of an AC current applied to a solenoid located under the sample. The vibration of $Fe_3O_4$ nanoparticles was detected by a nonmagnetic AFM tip to map the changes in frequency and amplitude of the vibrating sample at the level of individual $Fe_3O_4$ nanoparticles and clusters. Colloidal lithography was used to prepare patterns of $Fe_3O_4$ nanoparticles on a glass surface using basic steps of mixing, drying and removing the surface template of latex spheres. Monodisperse latex were used to guide the deposition of magnetic nanoparticles to collect in the spaces in between the close-packed spheres of the latex film. With a mixture approach of "two-particle" lithography, 2D arrays of patterned aggregates of metal nanoparticles were generated which formed a periodic, well-defined arrangement that was suitable for subsequent characterizations with magnetic sample modulation (MSM).

## Introduction

The size, shape, composition and properties of magnetic nanoparticles are critical design characteristics for potential applications. Magnetic nanoparticles have myriad uses ranging from high-density data storage,[1,2] nanoscale magnetic sensors,[3] nanoelectronics,[4] sensing,[5] magnetic information storage,[2] and magnetic refrigeration systems.[6] Magnetic nanoparticles have been applied in biological and biomedical assays and devices.[7,8] Nanoparticles are used as diagnostic tools in magnetic resonance imaging, magnetic separation of biological targets,[9] and as therapeutic agents for hyperthermic tumor treatments,[10, 11,12] as well as for targeted drug, and gene delivery.[13,14] The composition and shape of metal nanoparticles are key parameters which influence the corresponding size-dependent magnetic properties.[15-18]

Several strategies have been used to prepare assemblies of magnetic nanoparticles on planar substrates.[19,20,21] Forces such as hydrogen-bonding,[22] covalent bonding,[23] as well as electrostatic and van der Waals interactions[24] are involved in directing the assembly of nanoparticles.[25] Chemical patterning or surface electrostatic interactions have been used to prepare specifically patterned nanoparticle assemblies. Techniques that were used to deposit magnetic nanoparticles on substrates include gas phase deposition,[26] layer-by-layer assembly,[27] Langmuir-Blodgett techniques,[28, 29, 30] microcontact printing,[31] photolithography,[32] capillary filling,[31] drop-casting,[24] and self-assembly at the liquid-air interface.[33] Magnetic interactions were also used to assemble magnetic nanoparticles, in which an externally applied magnetic field was applied to control the local arrangement.[34,35,36] Structural patterns such as chains, and columns have been observed using magnetic field assisted methods.[37] Nanolithography technologies, such as e-beam lithography,[38,39] x-ray lithography,[40] optical lithography[41,42] and scanning probe-based lithography[43,44] also have been used to pattern magnetic nanoparticles.

Colloidal or particle lithography is a facile approach that has been used to pattern metal nanoparticles.[45-47] Particle lithography has been applied successfully to generate arrays of nanostructures of polymers,[48, 49] proteins,[50,51] metals,[52,53,54,55,56] quantum dots,[57,58,46] and self-assembled monolayers.[59,60] Particle lithography is based on simple steps of conventional bench chemistry procedures of mixing, centrifuging, evaporation and rinsing to produce arrays of nanomaterials. For particle lithography, monodisperse, spherical particles can serve as either a template or surface mask to form nanopatterns.

In our experiments, a strategy of "two-particle" lithography was developed to prepare periodic arrays of clusters of $Fe_3O_4$ nanoparticles as a well-defined test platform for scanning probe studies with magnetic sample modulation (MSM).[46] Atomic force microscopy (AFM) characterizations were accomplished with a hybrid imaging mode of atomic force microscopy, MSM-AFM.[61] The instrument configuration for MSM-AFM has been previously used for selective magnetic imaging of electrolessly deposited iron-oxide capped nanostructures formed on organosilane nanopatterns[61] and for imaging nanostructures of ferritin.[62] Relatively monodisperse, hydrophilic, and single-crystalline ferrite microspheres were prepared by a solvothermal reduction method by modified reduction reactions between $FeCl_3$ and ethylene glycol. Arrays of $Fe_3O_4$ nanoparticles on glass substrates exhibited a periodic arrangement, which span areas of microns. The density and surface coverage of the arrays can be controlled by selection of the diameters of the templating latex microspheres. The magnetic imaging mode of MSM-AFM is a variant of force modulation microscopy, however selectivity is achieved for magnetic samples that are caused to vibrate by an oscillating magnetic field.

## Experimental Section

### Materials and reagents

Glass substrates were acid cleaned by 1 h immersion in piranha solution. Piranha solution is a mixture of sulfuric acid (96%, EMD Chemical Inc., Gibbstown, NJ) and hydrogen peroxide (30%, Sigma-Aldrich) at a ratio of 3:1 (v/v). Piranha solution is highly corrosive and should be handled with caution using appropriate protective clothing, gloves and eyewear. Monodisperse latex spheres, 1 μm in diameter were obtained from Thermo Scientific, Waltham, MA. Ultrapure deionized water was used for cleaning glassware and preparing sample solutions from a MilliQ water system (Millipore Sigma, 18 MΩ•cm) to minimize contamination at the nanoscale.

### Synthesis of $Fe_3O_4$ nanoparticles

Our modified recipe of the procedure reported by Deng *et al* [63] yielded spherical $Fe_3O_4$ nanoparticles with diameters of 100, 125, and 135, nm. This involved charging a round bottom flask with iron chloride (1.4 g, $FeCl_3.6H_2O$) and sodium acetate (3.6 g) sequentially dissolved in 15 mL of ethylene glycol. Addition of sodium acetate rapidly turned the orange $FeCl_3.6H_2O$ solution to brown color. The solution was stirred for an additional 30 min and then injected at once into a round-bottomed flask containing a vigorously stirred solution of PVP (0.40 g) in 35 mL of ethylene glycol heated to 180 °C. The mixture was then vigorously stirred at 180 °C for 4–24 hours during which a black precipitate was obtained. The black precipitate was washed multiple times with ethanol, deionized water (18 megohm) and dried under vacuum at room temperature. Agitation (stirrer speed), temperature, and reaction time were the process parameters that were varied to obtain $Fe_3O_4$ nanospheres of desired diameters.

**Procedure for "two-particle" lithography**

Monodisperse latex spheres, 1 μm in diameter were mixed with $Fe_3O_4$ nanoparticles for "two-particle" lithography. The key steps are shown in Fig. 1. First, an aqueous solution of monodisperse latex was centrifuged at17000 rpm for 10 min to remove surfactants or other stabilizers. The pellet was then resuspended in the same volume of deionized water for one rinsing cycle by centrifugation. Next, the rinsed pellet of microspheres was resuspended in an aqueous solution containing $Fe_3O_4$ nanoparticles. A small volume (20 μL) of the mixture of nanoparticles and latex was placed onto a clean glass substrate. The droplet of sample was then dried in air at room temperature for at least 12 h. With ambient drying, monodisperse spheres spontaneously self-assemble to form close-packed arrangements on a flat surface. The smaller metal nanoparticles formed deposits within the exposed areas of the triple hollow sites in between latex spheres of the template. After the samples were dried, the larger microspheres were removed by gently pressing a piece of adhesive tape onto the sample and pulling off the latex film. During the tape removal step, the nanoparticles remained attached to the surface to form a patterned arrangement according to the periodicity of the latex template.

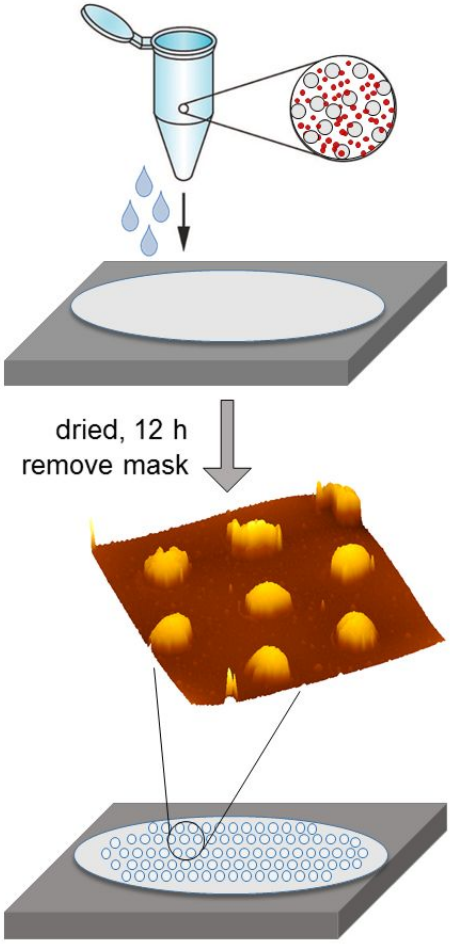


**Fig. 1** Basic steps for preparing $Fe_3O_4$ nanoparticles using "two-particle" lithography. A mixture of latex spheres and nanoparticles was deposited on the substrate. After drying the sample, the template was removed with adhesive tape to reveal a periodic arrangement of $Fe_3O_4$ nanoparticle clusters.

## Atomic Force Microscopy

Samples were characterized with a model 5500 scanning probe microscope (Keysight Technologies, Santa Rosa, CA). Nonconductive V-shaped cantilevers made of silicon nitride were used for imaging samples, which had low spring constants ranging from 0.1 to 0.5 $Nm^{-1}$ (Veeco Probes, Santa Barbara, CA). A plastic nosecone assembly without metal components and a magnetic AC mode (MAC-mode) sample plate were used for mounting probes on the scanner for MSM-AFM. Images were processed with Gwyddion, which is freely available as open source software supported by the Czech Metrology Institute.[64]

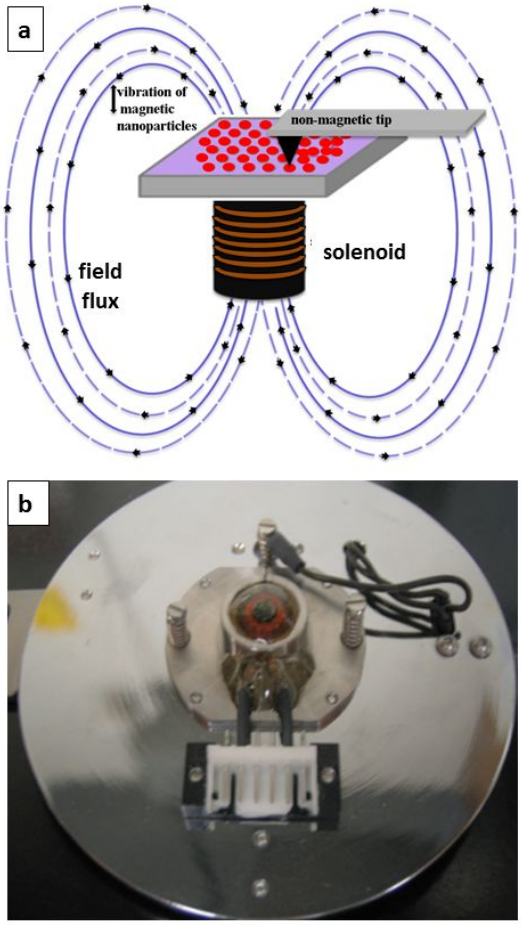


**Fig. 2** Instrument set-up for magnetic sample modulation AFM. (a) An AC magnetic field induces actuation of magnetic nanoparticles on a surface. A soft, nonmagnetic tip is operated in contact mode as a force and motion sensor. (b) Photo of the wire coil solenoid embedded within the sample plate.

The MSM-AFM setup is a hybrid of contact-mode AFM combined with selective actuation of magnetic samples (Fig. 2a).[61] First, the sample was scanned in contact-mode without applying the electromagnetic field, for acquiring conventional topography and lateral force images. For the second pass of the same area, an alternating electromagnetic field was applied with field strengths ranging between 0.01 to 0.2 T. Only the magnetic domains were driven to vibrate when an alternating electromagnetic field was applied to samples. The motion of samples was sensitively detected by amplitude and phase signals which were acquired simultaneously with MSM-topography frames. The magnetic field was applied using a MAC-mode sample stage shown in Fig. 2b which has a solenoid placed directly under the sample. Unlike the configuration

of MAC-mode imaging which uses a tip coated (underside) with a magnetic film for magnetically actuated tapping mode, the MSM set-up requires a nonconductive AFM probe. For MSM-AFM studies the stage was used to drive the vibration of the sample, rather than actuating the probe.

## Results and discussion

### Nanopatterns of $Fe_3O_4$ nanoparticles visualized with contact-mode AFM

Initial characterizations of the array of $Fe_3O_4$ nanoparticle clusters were obtained using contact-mode AFM (Fig. 3). Clusters of $Fe_3O_4$ nanoparticles as well as individual nanoparticles in a few areas between the clusters were observed in topography frames, an example is presented in Fig. 3a. In previous studies with "two-particle" lithography, we have prepared ring arrangements of smaller nanoparticles with diameters less than 20 nm.[46] Ring arrangements of ferritin, a spherical protein measuring ~12 nm in diameter were also prepared successfully using the mixture approach of "two-particle" lithography.[62] For the sample shown in Fig. 3, the $Fe_3O_4$ nanoparticles measured sizes ranging from 70 to 100 nm, which would be too large to fit in the meniscus sites at the base of latex spheres to generate ring arrangements. Instead, the metal nanoparticles filled the void spaces in between close packed spheres to form a periodic pattern of aggregates with spacing matching the distance between the microspheres of the latex template.

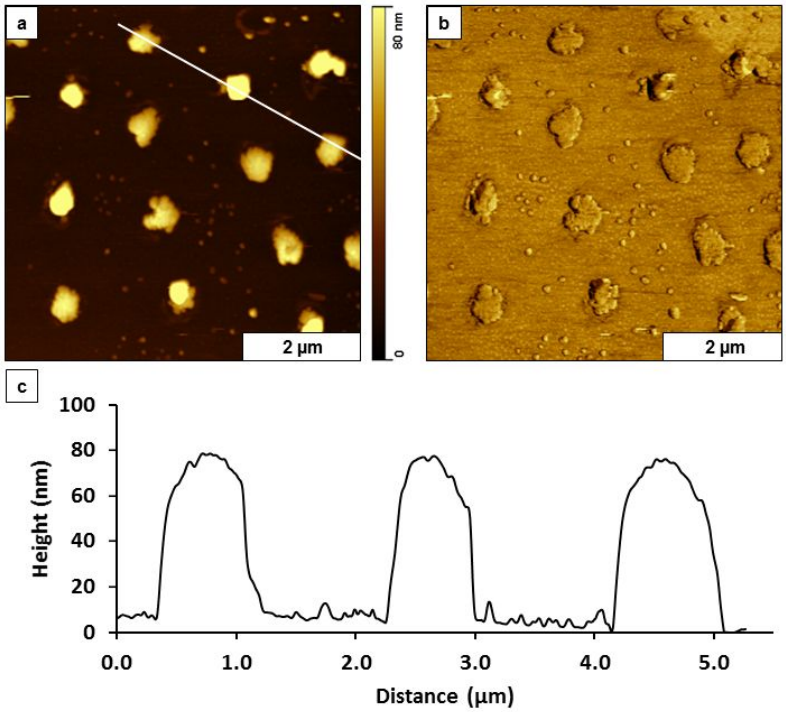


**Fig. 3** Clusters of magnetic $Fe_3O_4$ nanoparticles prepared on a glass substrate viewed with contact mode AFM images. (a) Arrangement of clusters of nanoparticles viewed with the topography channel; (b) corresponding lateral force image; (c) height profile for the white line in ***a*.**

The shapes and locations of the $Fe_3O_4$ clusters as well as smaller individual nanoparticles can be resolved in the simultaneously acquired lateral force image (Fig. 3b). The presence of smaller nanoparticles in areas between the clusters is more clearly viewed in the lateral force frame which discloses the shapes of the edges of the aggregates as well as the scattered arrangement of individual, isolated nanoparticles between the clusters. The height of three nanoparticle clusters measured using the substrate as a baseline is plotted in Fig. 3c, referencing the white line in Fig. 3a. The average height of the nanoparticle clusters measured 78 ± 10 nm from an average of 100 data points. Each $Fe_3O_4$ nanoparticle cluster is spaced approximately 1 µm apart, corresponding to the size of the latex microspheres used for patterning (1 µm diameter).

**Selective actuation of magnetic samples using MSM-AFM**

The test sample of nanopatterned clusters and $Fe_3O_4$ nanoparticles were imaged with and without an applied electromagnetic field, as shown in Fig. 4. Simultaneously acquired topography, MSM-amplitude and MSM-phase frames, respectively are presented for a 6 × 6 $\mu m^2$ area of the surface (Fig. 4). When the oscillating magnetic field was turned off there are no features or shapes evident in the amplitude or phase channels (top row, Figs. 4a, 4b, 4c). In the absence of a magnetic field the nanoparticles do not vibrate, therefore the amplitude and phase channels reveal no discernable features.

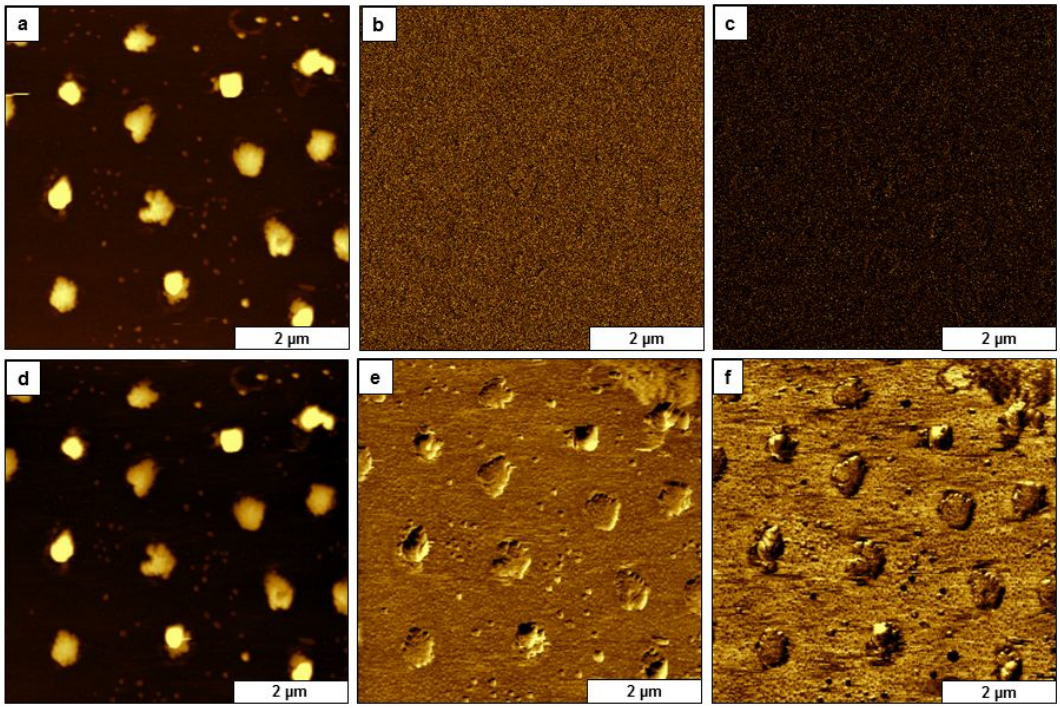


**Fig. 4** Clusters of $Fe_3O_4$ nanoparticles prepared on glass imaged with and without an applied electromagnetic field using MSM-AFM. Images in the top row were acquired in the absence of magnetic field: (a) Topography image; simultaneously acquired (b) amplitude; and (c) phase image. The bottom row of frames were acquired with an applied AC electromagnetic field: (d) Topography image; (e) corresponding MSM-amplitude; and (f) MSM-phase channels.

During the scan when the AC current is turned on to generate the flux of a magnetic field, the magnetic areas of the sample are induced to vibrate. For MSM-AFM, a continuously scanning tip operated in contact mode was placed on a sample that was driven to oscillate following the periodicity of the sinus AC waveform applied to the solenoid. The motion of the tip that is responding to the vibrating areas of the sample can be tracked using a lock-in amplifier, to generate images of changes in the motion of the AFM probe. The applied AC waveform was used as a reference for lock-in detection. Topography images were acquired concurrently with MSM amplitude and phase images (Figs. 4d, 43, 4f). For this example, comparing the topography frames with (Fig. 4a) and without (Fig. 4d) an applied field does not reveal any discernable changes because the motion is quite small. The two topography frames are mostly identical. However, tiny changes of tip motion caused by sample vibration are sensitively mapped in the amplitude and phase frames with MSM (Figs. 4e and 4f). In the concurrently acquired amplitude and phase images, deflection of the tip in the vertical direction is caused by the up and down motion of the nanomaterials responding to the flux of the applied field. The overall magnitude of the z deflection of the AFM probe caused by vibration of nanoparticles ranges from 1 to 4 nm and depends on the size of the surface feature.[61]

**Dynamic changes in MSM-AFM images with frequency**

Experimental parameters such as the driving frequency and applied field strength for MSM imaging can be optimized based on the information obtained from frequency sweeps. A frequency sweep can be acquired with MSM-AFM by placing the AFM tip directly on a vibrating nanoparticle cluster and measuring the amplitude as the frequency is ramped (Fig. 5). When the probe is placed on the substrate in areas where there is no magnetic sample, the frequency sweep is a flat line. The frequencies we selected include the prominent resonance peak

at 60.04 kHz and the small shoulder peak shown at 56.48 kHz. No prominent peaks were detected for the region of 100-400 kHz. The profile of a single resonance suggests that the nanocluster is oscillating as a solid block rather than having multiple vibrating domains. As samples are scanned with MSM-AFM, parameters such as the field strength and driving frequency can be evaluated to optimize resolution.

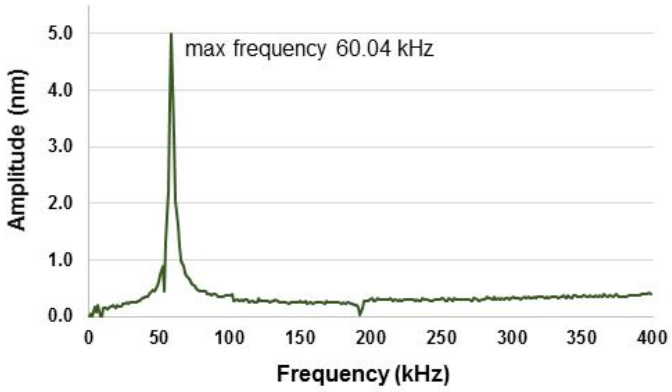


**Fig. 5** Spectra of a frequency sweep obtained by placing the AFM probe on a vibrating $Fe_3O_4$ nanocluster.

Results with MSM-AFM were acquired using two frequencies selected from the spectra of Fig. 5, with an applied average field strength of about 0.12 T as shown in Fig. 6. Changing the frequency at selected intervals during data acquisition of an MSM-AFM image enables a side-by-side evaluation of the vibrating nanoparticle clusters with chosen parameters (Fig. 6A, top row). The frequencies were changed *in situ* during a scan without halting data acquisition. The topography frame of Fig. 6A does not show any noticeable differences in morphology during the scan as the frequency parameter was changed *in situ*, however, the simultaneously acquired amplitude and phase channels reveal distinct changes as the frequency was ramped to 56.48 and 60.04 kHz. The scan was acquired with a line-by-line raster pattern from top to bottom with 512 lines/frame. At frequency 0 kHz there was no vibration of the $Fe_3O_4$ nanoparticle clusters, shown

in the upper portion of the frames of Fig. 6A. The uppermost part of the amplitude and phase channels do not display the shapes or locations of the nanoparticle clusters which are apparent in the concurrent topography image without an applied field. Mapping of magnetic domains was initiated when the frequency was increased to 56.48 kHz, as evident in the middle portion of the MSM-amplitude and MSM-phase images of Fig. 6A. As the frequency was changed incrementally during image acquisition with MSM-AFM, the vibrational amplitude of the sample changed accordingly. Interestingly, the much smaller individual nanoparticles also become visible at higher frequency in the MSM frames. For the frames acquired at 56.48 kHz improvements in the resolution of the phase image (right panel) are apparent with clearly defined edges and shape outlines. Thus, the resolution of phase images does not necessarily improve with higher amplitude response. At the resonance frequency of 60.04 kHz, magnetic features are apparent for both the amplitude and phase frames shown in the lower portion of Fig. 6A. In the frequency sweep of Fig. 5, the maximum amplitude response was detected at 60.04 kHz. Correspondingly, the best resolution for the amplitude frames was detected at the resonance frequency. This indicates that at resonance, the probe had a greater vertical displacement attributable to stronger sample vibration.

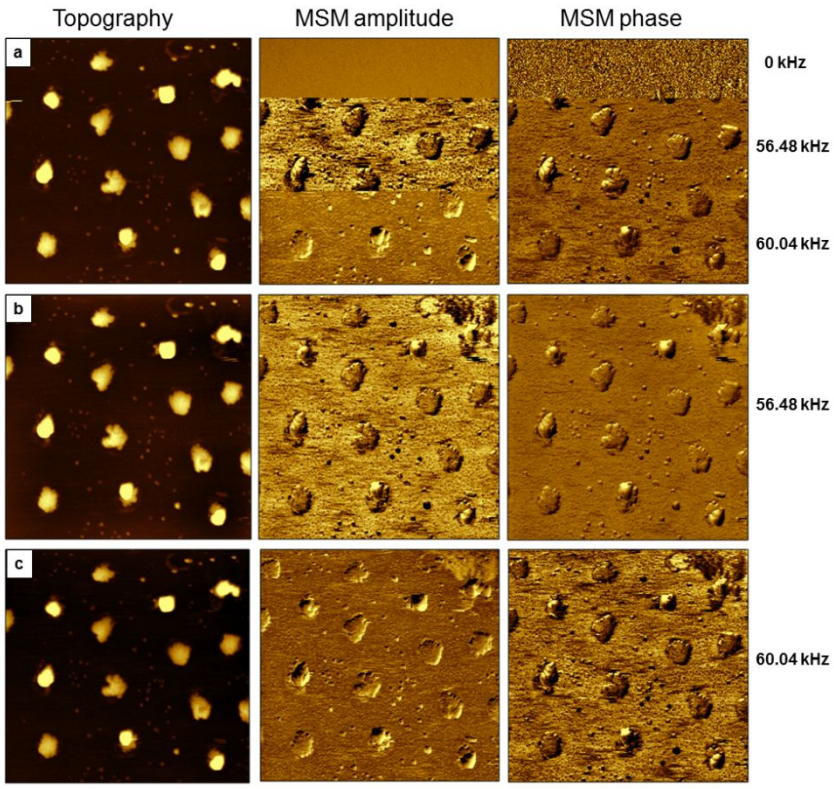


**Fig. 6** Magnetic nanoparticle clusters of $Fe_3O_4$ prepared on glass imaged at selected frequencies. (a) The top row indicates changes for images as the frequency was changed *in situ*. From left to right, topography, amplitude and phase channels are shown for a 5 × 5 $um^2$ area. (b) Frames in the center row were acquired at a frequency of 56.48 kHz; (c) Images in the bottom row were acquired at a resonance frequency of 60.04 kHz.

Images of the sample of $Fe_3O_4$ nanoparticle clusters acquired with the magnetic field actuated at a single frequency throughout the entire scan are shown in Figs. 6b-6c. Note that the topography frames (left images) are comparable when scanning the same area regardless of the selected frequency parameters. The topography frames of Figs. 6a, 6b and 6c are unchanged when a field is applied, there are no visible differences between the three images. We have observed side-to-side physical motion of samples in topography frames previously with studies of ferritin,[62] however for the $Fe_3O_4$ samples prepared on a glass substrate, the physical motion in the lateral direction was too small to distinguish in topographs. Small changes in the up-down motion of the tip-surface contact were compared to the driving signal and the differences detected by the lock-in amplifier are plotted digitally with amplitude and phase channels to

generate surface maps of magnetic response (Figs. 6b and 6c). Amplitude and phase channels are compared side-by-side for the chosen frequencies in the center and left hand columns, respectively in Fig. 6. For these examples, the ultra-fine details of the shapes and locations of small adsorbates in between the larger clusters are revealed by MSM amplitude and phase images. The smallest features are not discernable in the topography frames due to the saturation and convolution of the height color scale. Both of the frequencies selected (56.48 and 60.04 KHz) were suitable for successful imaging with MSM-AFM.

**Effect of magnetic field strength for the resolution of MSM-AFM images**

Example topography, amplitude, and phase images acquired concurrently with changes in the applied magnetic field were captured *in situ* within a single MSM-AFM frame in Fig. 7. The tip-sample resonance frequency was maintained at 60.04 kHz during acquisition. Within a single scan, the magnetic field strength was changed from 0 T, 0.05 T, and 0.12 T respectively, without halting data acquisition. The topography frame in Fig. 7a, does not show significant differences in image resolution as the field strength was increased from top-to-bottom of the scan. The MSM amplitude (Fig. 7b) and MSM phase (Fig. 7c) channels sensitively reveal the location of $Fe_3O_4$ nanoparticles and clusters arranged on the glass surface only when the field was activated. When the field strength was 0 T, no vibrations were detected in the upper region of Figs. 7b and 7c. However, as the field strength was increased to 0.05 T, the vibration of nanoparticles become apparent. As the field strength was further increased to 0.12 T, the amplitude of the vibrating nanoparticle clusters increased as shown by sharper contrast in the bottom portion of the MSM amplitude and MSM phase images. As the magnetic field strength was increased, smaller individual nanoparticles surrounding the clusters can be resolved in the MSM amplitude and phase channels.

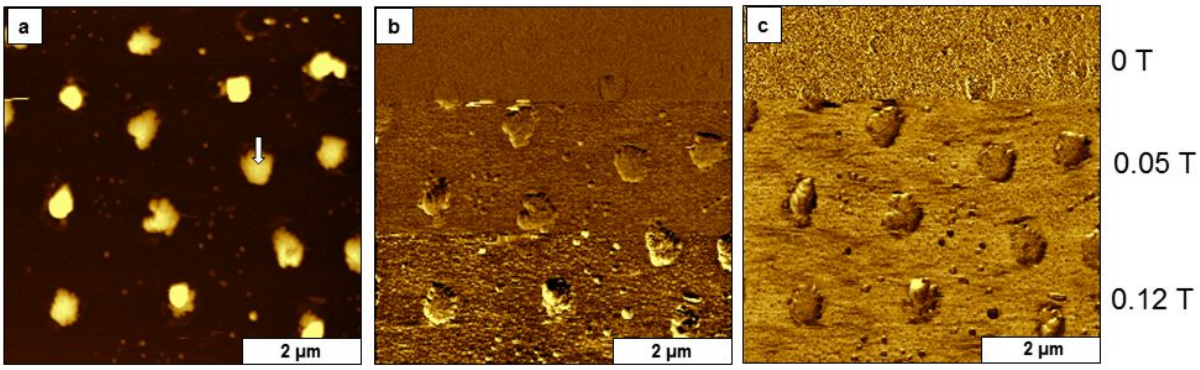


**Fig. 7** Changes for MSM images as the strength of the applied electromagnetic field was ramped. (a) Topography frame acquired in ambient air. The white arrow in the topography image indicates the location where the AFM tip was placed on a $Fe_3O_4$ nanoparticle cluster for the spectra of Fig. 8. (b) Simultaneously acquired MSM amplitude and (c) MSM phase channels.

The capability of MSM to map magnetic domains with dynamic parameters is demonstrated in Fig. 7. Information about the location and relative vibrational response of the magnetic domains can be acquired. As the magnetic field strength is ramped, particles can be shaken loose from the substrate and displaced with the scanning motion of the tip as it is operated in contact-mode. Therefore, in conducting experiments we begin with lower field strengths and increase the parameter to evaluate an optimum setting. Phase images present the fine details of surface shapes, such as for defining the boundaries and lateral dimensions of nanoparticle cluster. Depending on the size of the nanoparticles, smaller nanomaterials can be detected at higher field strengths, as revealed in the MSM-amplitude and MSM-phase channels. We have observed that as nanoparticles decrease in size, a stronger field is required to induce vibration. Very small nanoparticles may not be detectable with smaller field strengths, depending on the nature of surface attachment. For strongly bonded nanoparticles or samples with embedded nanoparticles, vibration cannot be detected with MSM-AFM. Interestingly, nanoparticles that are vaguely distinguished or even invisible in the topography image are readily visualized in MSM amplitude and phase frames.

A comparison of frequency profiles acquired in a selected sample location when the probe was placed directly on top of a nanoparticle cluster is shown in Fig. 8. Essentially, the AFM tip was parked on a single nanoparticle cluster and frequency spectra were acquired at selected field strengths. An overlay of the amplitude vs frequency spectra with incremental changes in the field strength exhibited neatly symmetric peak profiles, which reveal the primary resonance frequency at 60.04 kHz.

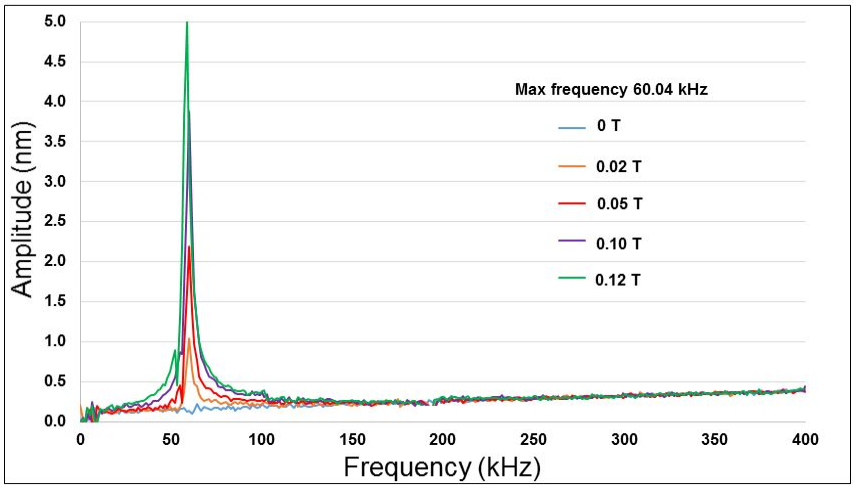


**Fig. 8** Overlay of MSM frequency spectra acquired with a tip placed on a single cluster of $Fe_3O_4$ nanoparticles as the field strength was ramped.

The amplitude axis of Fig. 8 indicates the z displacement of the AFM tip, and ranged from 0 to 5.0 nm for this experiment. Typically, the spectra will reveal a prominent resonance peak and multiple smaller peaks, depending on the complexity of the sample. The amplitude peak height increased proportionately as the field strength was ramped. An amplitude response of 2.3 nm was observed when the applied field was set at 0.05 T and a higher amplitude response of 5.0 nm was attained when the magnetic strength was increased to 0.12 T. There is a second peak which appears as a shoulder to the maxima peak, which occurs at 56.48 kHz. This

resonance was also successful as an experimental parameter for MSM-AFM imaging of $Fe_3O_4$ nanoparticles (Fig. 6b).

## Conclusion

Studies with MSM-AFM provide detailed information of the response of isolated and clusters of magnetic nanoparticles under the flux of an externally applied AC electromagnetic field. Isolated nanoparticles that are invisible in topography frames can be sensitively mapped with MSM imaging. Magnetic $Fe_3O_4$ nanoparticles were patterned on glass substrates for studies with MSM-AFM. Patterning was accomplished with colloidal lithography using polymeric beads as a structural template to define areas for depositing smaller-sized $Fe_3O_4$ nanoparticles on a glass surface. Information of the location of individual magnetic domains can be detected with MSM-AFM, the nanoparticles vibrate in response to the flux of an AC electromagnetic field generated by a solenoid placed directly under the sample. Spectra of the characteristic resonance frequencies of the $Fe_3O_4$ nanoparticle clusters can be acquired reproducibly while the tip is placed in contact with an individual cluster of nanoparticles. Dynamic studies with MSM-AFM revealed an increase in the vibration amplitude when ramping the strength of the applied magnetic field. The resonance profiles of the frequency spectra are not identical for nanoparticles of different sizes, further experiments are being designed to systematically evaluate the size-dependent resonance profiles for nanoparticles according to changes in size, shape and composition. Future studies will include imaging mixtures of metal nanoparticles with different composition and size to evaluate the resonance signatures in response to an applied magnetic field.

## Author information

Corresponding Author

*E-mail: jgarno@lsu.edu

## Conflicts of interest

There are no conflicts to declare.

## Acknowledgements

We gratefully acknowledge support from the National Science Foundation Career/PECASE award (CHE-0847291) and the Louisiana Board of Regents Support fund (LEQSF(2014-16)-ENH-TR-03).

## References


1. J. Martın, J. Nogues, K. Liu, J. Vicent and I. K. Schuller, *J. Magn. Magn. Mater.*, 2003, **256**, 449-501.
2. B. D. Terris and T. Thomson, *J. Phys. D*, 2005, **38**, R199.
3. S. Sun, C. B. Murray, D. Weller, L. Folks and A. Moser, *Science*, 2000, **287**, 1989-1992.
4. B. Yu and M. Meyyappan, *Solid-State Electron.*, 2006, **50**, 536-544.
5. A. N. Shipway, E. Katz and I. Willner, *ChemPhysChem*, 2000, **1**, 18-52.
6. S. Mørup, *Hyperfine Interact*, 1994, **90**, 171-185.
7. J. Gao, H. Gu and B. Xu, *Acc. Chem. Res.*, 2009, **42**, 1097-1107.
8. A. K. Gupta and M. Gupta, *Biomaterials*, 2005, **26**, 3995-4021.
9. Y.-w. Jun, J.-w. Seo and J. Cheon, *Acc. Chem. Res.*, 2008, **41**, 179-189.
10. A. Hervault and N. T. K. Thanh, *Nanoscale*, 2014, **6**, 11553-11573.
11. T. Pedro, M. María del Puerto, V.-V. Sabino, G.-C. Teresita and J. S. Carlos, *J. Phys. D*, 2003, **36**, R182.
12. R. Banerjee, Y. Katsenovich, L. Lagos, M. McIintosh, X. Zhang and C. Z. Li, *Current Med. Chem.*, 2010, **17**, 3120-3141.
13. S. Laurent, D. Forge, M. Port, A. Roch, C. Robic, L. Vander Elst and R. N. Muller, *Chem. Rev.*, 2008, **108**, 2064-2110.
14. C. B. Catherine and S. G. C. Adam, *J. Phys. D*, 2003, **36**, R198.
15. A. Demortiere, P. Panissod, B. P. Pichon, G. Pourroy, D. Guillon, B. Donnio and S. Begin-Colin, *Nanoscale*, 2011, **3**, 225-232.
16. T.-J. Park, G. C. Papaefthymiou, A. J. Viescas, A. R. Moodenbaugh and S. S. Wong, *Nano Lett.*, 2007, **3**, 766-772.
17. J. P. Wilcoxon and B. L. Abrams, *Chem. Soc. Rev.*, 2006, **35**, 1162-1194.
18. J. Bansmann, S. H. Baker, C. Binns, J. A. Blackman, J. P. Bucher, J. Dorantes-Davila, V. Dupuis, L. Favre, D. Kechrakos, A. Kleibert, K. H. Meiwes-Broer, G. M. Pastor, A. Perez, O. Toulemonde, K. N. Trohidou, J. Tuaillon and Y. Xie, *Surf. Sci. Rep.*, **56**, 189-275.
19. S. Bedanta, A. Barman, W. Kleemann, O. Petracic and T. Seki, *J. Nanomater.*, 2013, **2013**, 22.
20. S. Kinge, M. Crego-Calama and D. N. Reinhoudt, *ChemPhysChem*, 2008, **9**, 20-42.
21. J. I. Martín, J. Nogués, K. Liu, J. L. Vicent and I. K. Schuller, *J. Magn. Magn. Mater.*, 2003, **256**, 449-501.
22. E. Hao and T. Lian, *Langmuir*, 2000, **16**, 7879-7881.

23. C. Lu, N. Wu, X. Jiao, C. Luo and W. Cao, *Chem. Comm.*, 2003, **9**, 1056-1057.
24. S. Disch, E. Wetterskog, R. P. Hermann, G. Salazar-Alvarez, P. Busch, T. Brückel, L. Bergström and S. Kamali, *Nano Lett.*, 2011, **11**, 1651-1656.
25. W. H. Binder, *Angew. Chem. Int. Ed.*, 2005, **44**, 5172-5175.
26. C. Binns, K. N. Trohidou, J. Bansmann, S. H. Baker, J. A. Blackman, J. P. Bucher, D. Kechrakos, A. Kleibert, S. Louch, K. H. Meiwes-Broer, G. M. Pastor, A. Perez and Y. Xie, *J. Phys. D*, 2005, **38**, R357.
27. D. Grigoriev, D. Gorin, G. B. Sukhorukov, A. Yashchenok, E. Maltseva and H. Möhwald, *Langmuir*, 2007, **23**, 12388-12396.
28. M. Pauly, B. P. Pichon, P.-A. Albouy, S. Fleutot, C. Leuvrey, M. Trassin, J.-L. Gallani and S. Begin-Colin, *J. Mater. Chem.*, 2011, **21**, 16018-16027.
29. F. Mammeri, Y. L. Bras, T. J. Daou, J.-L. Gallani, S. Colis, G. Pourroy, B. Donnio, D. Guillon and S. Bégin-Colin, *J. Phys. Chem. B*, 2009, **113**, 734-738.
30. C. Liu, Y. Shan, Y. Zhu and K. Chen, *Thin Solid Films*, 2009, **518**, 324-327.
31. S. Palacin, P. C. Hidber, J.-P. Bourgoin, C. Miramond, C. Fermon and G. M. Whitesides, *Chem. Mater.* , 1996, **8**, 1316-1325.
32. T. Wen, D. Zhang, Q. Wen, H. Zhang, Y. Liao, Q. Li, Q. Yang, F. Bai and Z. Zhong, *Nanoscale*, 2015, **7**, 4906-4911.
33. A. Dong, J. Chen, P. M. Vora, J. M. Kikkawa and C. B. Murray, *Nature*, 2010, **466**, 474-477.
34. B. B. Yellen and G. Friedman, *Langmuir*, 2004, **20**, 2553-2559.
35. A. Snezhko and I. S. Aranson, *Nat. Mater.*, 2011, **10**, 698-703.
36. K. A. Mirica, F. Ilievski, A. K. Ellerbee, S. S. Shevkoplyas and G. M. Whitesides, *Adv. Mater.*, 2011, **23**, 4134-4140.
37. A. Joseph and S. Mathew, *ChemPlusChem*, 2014, **79**, 1382-1420.
38. S. Y. Chou, M. Wei, P. R. Krauss and P. B. Fischer, *J. Vac. Sci. Technol. B*, 1994, **12**, 3695-3698.
39. R. O'Barr, M. Lederman, S. Schultz, W. Xu, A. Scherer and R. J. Tonucci, *J. Appl. Phys.*, 1996, **79**, 5303-5305.
40. F. Rousseaux, D. Decanini, F. Carcenac, E. Cambril, M. F. Ravet, C. Chappert, N. Bardou, B. Bartenlian and P. Veillet, *J. Vac. Sci. Technol. B*, 1995, **13**, 2787-2791.
41. M. Thielen, S. Kirsch, H. Weinforth, A. Carl and E. F. Wassermann, *IEEE T. Magn.*, 1998, **34**, 1009-1011.
42. C. A. Ross, H. I. Smith, T. Savas, M. Schattenburg, M. Farhoud, M. Hwang, M. Walsh, M. C. Abraham and R. J. Ram, *J. Vac. Sci. Technol. B*, 1999, **17**, 3168-3176.
43. J. C. Garno, Y. Yang, N. A. Amro, S. Cruchon-Dupeyrat, S. Chen and G.-Y. Liu, *Nano Lett.*, 2003, **3**, 389-395.

44. L. Fu, X. Liu, Y. Zhang, V. P. Dravid and C. A. Mirkin, *Nano Lett.*, 2003, **3**, 757-760.
45. K. L. Lusker, J.-R. Li and J. C. Garno, *Langmuir*, 2011, **27**, 13269-13275.
46. B. R. Lewandowski, A. T. Kelley, R. Singleton, J.-R. Li, M. Lowry, I. M. Warner and J. C. Garno, *J. Phys. Chem. C*, 2009, **113**, 5933-5940.
47. J.-R. L. Li, K. L.; Yu, J. J.; Garno, J. C. ACS Nano, 2009, 3, 2023-2035. , *ACS Nano*, 2009, **3**, 2023-2035.
48. D.-G. Choi, H. K. Yu, S. G. Jang and S.-M. Yang, *Chem. Mater.*, 2003, **15**, 4169-4171.
49. Z. Sun, Y. Li, Y. Wang, X. Chen, J. Zhang, K. Zhang, Z. Wang, C. Bao, J. Zeng, B. Zhao and B. Yang, *Langmuir*, 2007, **23**, 10725-10731.
50. Y. Cai and B. M. Ocko, *Langmuir*, 2005, **21**, 9274-9279.
51. L. E. Englade-Franklin, C. K. Saner and J. C. Garno, *Interface Focus*, 2013, **3**.
52. F. Sun, W. Cai, Y. Li, G. Duan, W. T. Nichols, C. Liang, N. Koshizaki, Q. Fang and I. W. Boyd, *Appl. Phys. B*, 2005, **81**, 765-768.
53. B. J. Y. Tan, C. H. Sow, T. S. Koh, K. C. Chin, A. T. S. Wee and C. K. Ong, *J. Phys. Chem. B*, 2005, **109**, 11100-11109.
54. S. M. Weekes, F. Y. Ogrin, W. A. Murray and P. S. Keatley, *Langmuir*, 2007, **23**, 1057-1060.
55. S. M. Weekes, F. Y. Ogrin and W. A. Murray, *Langmuir*, 2004, **20**, 11208-11212.
56. J. Rybczynski, U. Ebels and M. Giersig, *Colloids Surface A*, 2003, **219**, 1-6.
57. Y. B. Zheng, S. J. Chua, C. H. A. Huan and Z. L. Miao, *J. Cryst. Growth*, 2004, **268**, 369-374.
58. J. Chen, W.-S. Liao, X. Chen, T. Yang, S. E. Wark, D. H. Son, J. D. Batteas and P. S. Cremer, *ACS Nano*, 2009, **3**, 173-180.
59. C. K. Saner, K. L. Lusker, Z. M. LeJeune, W. K. Serem and J. C. Garno, *Beilstein J. Nanotechnology*, 2012, **3**, 114-122.
60. M. Geissler, J. M. McLellan, J. Chen and Y. Xia, *Angew. Chem. Int. Ed.*, 2005, **44**, 3596-3600.
61. J.-R. Li, B. R. Lewandowski, S. Xu and J. C. Garno, *Anal. Chem.*, 2009, **81**, 4792-4802.
62. S. L. Daniels, J. N. Ngunjiri and J. C. Garno, *Anal. Bioanal. Chem.*, 2009, **394**, 215-223.
63. H. Deng, X. Li, Q. Peng, X. Wang, J. Chen and Y. Li, *Angew. Chem. Int. Ed.*, 2005, **44**, 2782-2785.
64. D. Necas and P. Klapetek, *centr.eur.j.phys.*, 2012, **10**, 181-188.

## Graphical abstract

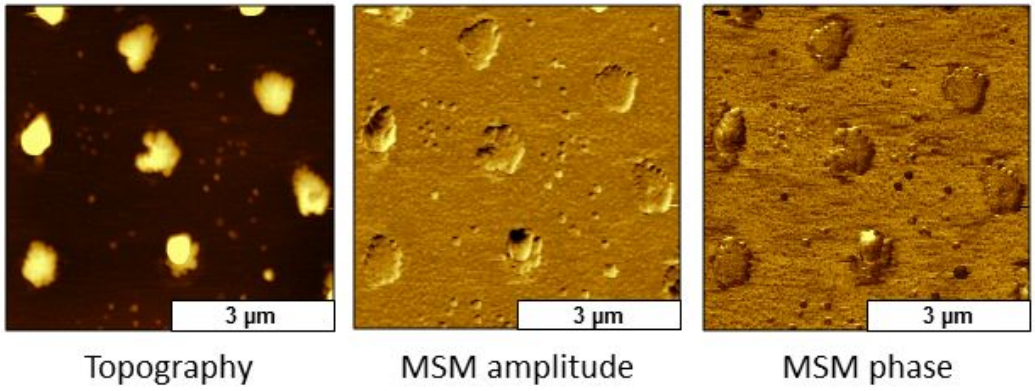


Example MSM-AFM images of $Fe_3O_4$ nanoparticles arranged on glass; individual nanoparticles are resolved in areas between patterns of aggregate assemblies.